

Surface-Confined Fabrication of Ultrathin Nickel Cobalt-Layered Double Hydroxide Nanosheets for High-Performance Supercapacitors

Juan Yang, Chang Yu, Chao Hu, Man Wang, Shaofeng Li, Huawei Huang, Karen Bustillo, Xiaotong Han, Changtai Zhao, Wei Guo, Zhiyuan Zeng, Haimei Zheng,* and Jiешan Qiu*

The design and fabrication of 2D nanostructure electrodes with desired electrochemical activities is highly demanded for electrocatalysis and supercapacitors. Herein, the tuned fabrication of ultrathin and tortuous nickel/cobalt-layered double hydroxide (NiCo-LDH) nanosheets via a graphene oxide (GO) surface-confined strategy is reported, yielding nanosheets with a thickness of 1.7–1.8 nm that is duplicated from the graphene oxides in terms of both the lateral size and the shape. It has been found that the C/O functional groups on the GO surface have functioned to promote the oxidation of Co^{2+} to Co^{3+} , and to transform the β -phase NiCo-hydroxide (NiCo-OH) into the LDH-phase with tuned homogenous composition and geometry. The ultrathin NiCo-LDH nanosheets mimic the morphology and size of the graphene due to the surface-confined and/or surface-guided growth. The as-obtained NiCo-LDH-graphene (NiCo-LDH-G) nanosheets exhibit a superior electrocatalytic activity for oxygen evolution reaction, evidenced by a small overpotential of 0.337 V (@10 mA cm^{-2} in 0.1 M KOH electrolyte), and a high charge storage capability of 1489 F g^{-1} as electrodes for supercapacitors. This 2D surface-confined growth strategy may pave a way for the fabrication of ultrathin 2D materials including but not limited to transition metal hydroxides for high-performance electrochemical applications.

1. Introduction

2D nanomaterials with fascinating physical and chemical properties hold great potential in many fields such as catalysis, electronics, energy-storage, and energy-conversion.^[1,2] In particular, ultrathin nanosheets with single-/few-atomic-layers, originated from metal-organic coordination frameworks (MOF), metal oxides/hydroxides and dichalcogenides (TMDs), are more attractive as electrocatalysts or energy-storage electrodes,^[3–5] evidenced by the results that this kind of ultrathin structure with all of the active sites being fully exposed, is capable of tuning the band gap energy and the density of states (DOS) near the Fermi level, which leads to high electrical conductivity.^[6–8] Moreover, these exposed metal ions that used to be coordinatively unsaturated, would function as highly active centers to decrease the energy barrier of the electrochemical reactions and to enhance the capture ability of electrolyte ions, which helps to further

Dr. J. Yang, Dr. C. Hu, M. Wang
School of Chemical Engineering and Technology
Xi'an Jiaotong University
Xi'an 710049, China

Prof. C. Yu, S. Li, H. Huang, X. Han, C. Zhao, W. Guo,
Prof. J. Qiu
State Key Lab of Fine Chemicals
School of Chemical Engineering
Liaoning Key Lab for Energy Materials and Chemical
Engineering
Dalian University of Technology
Dalian 116024, China
E-mail: jqiu@dlut.edu.cn

Dr. K. Bustillo
National Center for Electron Microscopy
Molecular Foundry
Lawrence Berkeley National Laboratory
Berkeley, CA 94720, USA

Dr. Z. Zeng
Materials Science Division
Lawrence Berkeley National Laboratory
Berkeley, CA 94720, USA

Prof. H. Zheng
Department of Materials Science and Engineering
University of California
Berkeley, CA 94720, USA
E-mail: hmzheng@lbl.gov

Prof. H. Zheng
Materials Science Division
Lawrence Berkeley National Laboratory
Berkeley, CA 94720, USA

Prof. J. Qiu
College of Chemical Engineering
Beijing University of Chemical Technology
Beijing 100029, China

 The ORCID identification number(s) for the author(s) of this article can be found under <https://doi.org/10.1002/adfm.201803272>.

DOI: 10.1002/adfm.201803272

improve the electrochemical reaction kinetics within the electrode matrix.

To fabricate 2D ultrathin nanosheets with attractive properties, a number of strategies have been developed, including bottom-up synthesis by epitaxial growth and chemical vapor deposition (CVD),^[9–11] and top-down strategies by physical and/or chemical liquid exfoliation.^[2,12] However, the techniques available now are usually hindered by harsh growth conditions (e.g., high temperature and relatively high vacuum), low synthetic yield, or complicated and time-consuming steps that limit the large-scale synthesis of materials for practical use. It is desirable to develop a simple yet cost-effective approach to achieve controlled fabrication of the promising ultrathin nanosheets.^[4,13–16] For example, Xie et al. demonstrated the fabrication of ultrathin β -Co(OH)₂ nanosheets with a single layer of five atoms by an oriented-attachment strategy,^[8] resulting in nanosheet electrodes with a large storage capacitance and superior rate capability for supercapacitors. Zhang et al. have developed an inverse microemulsion technique to fabricate ultrathin ZnAl layered double hydroxide (ZnAl-LDH) nanosheets that have more surface defects, and exhibit extraordinarily high electrochemical activity for the reduction of carbon dioxide to carbon monoxide in comparison to bulky LDH.^[6] Song and Hu fabricated ultrathin CoMn-LDH nanosheets by a one-pot coprecipitation method at room temperature that showed a high activity and robust stability after electrochemical anodic conditioning for the oxygen evolution reaction (OER).^[17] Nevertheless, the controllable fabrication of ultrathin nanosheets still remains a challenge as most of the strategies available now have some limits in terms of the quality of nanosheets either with small lateral size or unsatisfying structure flexibility.

One of the unique functions of the 2D graphene oxides (GO) is capable of guiding the growth/self-assembly of various inorganic materials, leading to integrated composite nanosheets with controlled universal size and good structural stability.^[18–20] Moreover, the morphology effect on the scalability of graphene endows the 2D composite nanosheets with highly tortuous structures, which further guarantee unimpeded ion transport channels inside the electrodes. However, these composite nanosheets, usually with the common hybrid structures and/or inorganic nanoparticles being loaded onto the graphene surfaces,^[18,21–23] do not always duplicate the graphene structure

perfectly, which consequently lead to unsatisfied electrochemical performance. In this regard, the fabrication of ultrathin and highly tortuous inorganic nanosheets with excellent electrochemical activity remains a bottleneck to be tackled.

In the present work, we have fabricated ultrathin and highly tortuous NiCo-LDH nanosheets that have duplicated the structure and lateral size of the graphene via the GO surface-confined strategy. The C/O functional groups on the GO surface function as oxidation sites to promote the formation of Co³⁺ ions, and to induce transformation of the NiCo-hydroxides (NiCo-OH) from the β -phase to the LDH-phase. The surface-confined and/or surface-guided growth of the NiCo-LDH nanosheets on graphene is triggered by a unique electrostatic field between the as-formed host layers of LDH and the GO surface, yielding the ultrathin NiCo-LDH-graphene (NiCo-LDH-G) nanosheets with the highly tortuous structure that show superior performance as electrocatalysts for the OER and as electrodes for supercapacitors.

2. Results and Discussion

2.1. Fabrication of Ultrathin NiCo-LDH-G Nanosheets

The fabrication process of ultrathin and tortuous NiCo-LDH-G nanosheets is illustrated in **Figure 1**. In the absence of GO, free nucleation and growth of NiCo-hydroxide (NiCo-OH) would take place, as shown in Figure 1i, resulting in bulky plates made of some α -phase and mostly β -phase with an interlayer spacing of ≈ 4.6 Å.^[24] While in the presence of GO, ultrathin and highly tortuous NiCo-LDH nanosheets are formed in the aqueous solution, showing the unique role of the GO. First, the C/O functional groups, such as carboxyl (–COOH), carbonyl (–C=O), hydroxy (–C–OH), and epoxy group on the GO surface (Figure S1 and Table S1, Supporting Information), are helpful to the oxidation of Co²⁺ to Co³⁺ ions. Then, the Co³⁺ ions coprecipitate with Ni²⁺ and the remaining unoxidized Co²⁺ ions, resulting in a 2D material NiCo-LDH that is made of positively charged host layers with edge-sharing MO₆ octahedra (M represents divalent and trivalent metal ions). The edge-sharing octahedral building blocks result in the infinite 2D sheets, where each metal ion is six-fold coordinated by –OH groups. Importantly,

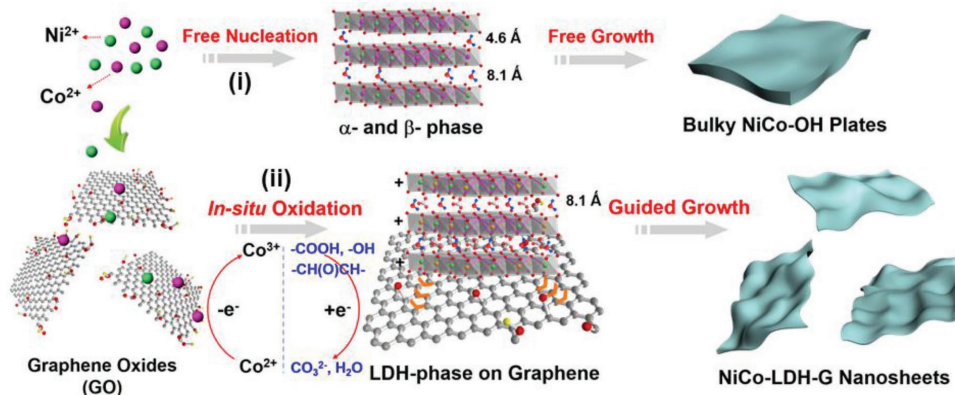


Figure 1. Schematic illustration of the fabrication routes of NiCo-LDH-G nanosheets. i) The growth process of NiCo-hydroxide (NiCo-OH) in the absence of GO, leading to the bulky and rigid NiCo-OH plates with the main interlayer spacing of ≈ 4.6 Å; ii) GO surface-guided growth of NiCo-LDH nanosheets, yielding ultrathin and highly tortuous NiCo-LDH-G nanosheets with an interlayer spacing of ≈ 8.1 Å.

the inherently and relatively wide interlayer spacing ($\approx 8.1 \text{ \AA}$) of the LDH nanostructures, in comparison to $\approx 4.6 \text{ \AA}$ of traditional metal hydroxides (especially β -phase hydroxides), will allow electrolyte ions and water molecules to get access to the active sites quickly and efficiently. These interlayer regions could act as "ion-buffering reservoirs" of the aqueous electrolyte to speed up the electrochemical reactions.^[25] Finally, owing to the unique electrostatic interaction between the LDH and GO (positively charged host layers vs negatively charged surface), the surface-confined growth of the NiCo-LDH nanosheets in the nanoscale dimension occurs under a reflux condition. The NiCo-LDH nanosheets are homogeneous and fully coated on the graphene, yielding ultrathin and highly tortuous NiCo-LDH-G nanosheets. This GO surface-confined growth approach has overcome the disadvantages and difficulties of forming ultrathin nanosheet structures by conventional liquid-based exfoliating methods. It should be noted that this fabrication process is rarely presented in the 2D layered materials as reported previously.^[19,26–28]

Figure 2 shows the structural characterization results of bulky NiCo-OH and NiCo-LDH-G nanosheets. The powder X-ray diffraction (XRD) patterns of the bulky NiCo-OH plates and ultrathin NiCo-LDH-G nanosheets are shown in Figure 2a. The main diffraction peaks of the NiCo-OH plates at 2θ of

18.8°, 32.7°, 38.0°, and 51.4° corresponding to (001), (100), (101), and (102) planes of the β -phase hydroxides can be clearly seen. In addition, several relatively weak peaks in the NiCo-OH samples can be well indexed to α -phase hydroxides,^[29] of which the fraction is $\approx 18.9\%$ estimated by the strongest peak intensity ratio of the two phases. This implies that the as-obtained bulky NiCo-OH plates are mainly composed of β -phase hydroxides. It is interesting to note that the diffraction peaks of the NiCo-LDH-G nanosheets have an obvious change in comparison to that of bulky NiCo-OH plates, these characteristic diffraction peaks belong to 2D hydrotalcite-like materials, implying the formation of LDH phase. It is noted that the diffraction peak at 2θ of 10.0° corresponding to GO (Figure S2, Supporting Information) in the NiCo-LDH-G nanosheets disappears completely after the refluxing reaction. The Raman results further confirm the presence of graphene, in which two characteristic peaks of the D and G bands at ≈ 1350 and 1580 cm^{-1} can be found (Figure S3, Supporting Information). Compared with the pristine graphene sheets obtained under the same conditions, the I_D/I_G ratio of the NiCo-LDH-G nanosheets increases slightly from 1.04 to 1.11, which is mainly related to more structure defects after the coating of NiCo-LDH on the graphene surface.^[30]

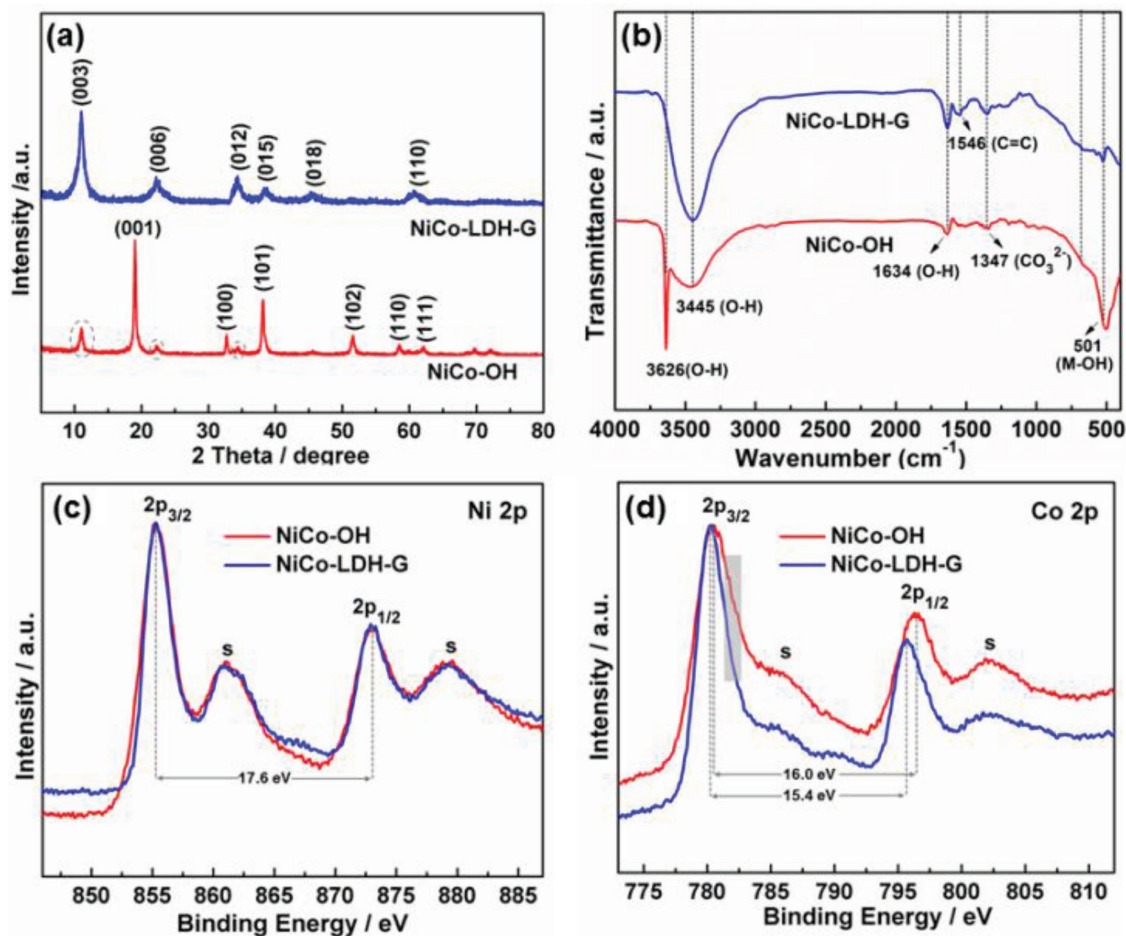


Figure 2. Structure characterization of the as-prepared samples: a) XRD patterns and b) FT-IR spectra of the bulky NiCo-OH plates and ultrathin NiCo-LDH-G nanosheets; c) Ni 2p and d) Co 2p high-resolution XPS spectra of the bulky NiCo-OH plates and ultrathin NiCo-LDH-G nanosheets.

Figure 2b shows the Fourier transform infrared (FT-IR) spectra of the bulky NiCo-OH and NiCo-LDH-G nanosheets, in which a sharp peak at 3626 cm^{-1} from the NiCo-OH plates can be attributed to the free $-\text{OH}$ groups of the typical β -phase hydroxides.^[29,31] The broad peaks centering at 3445 and 1634 cm^{-1} are assigned to the O–H stretching vibration of interlayer water molecules. The weak peaks at 1347 cm^{-1} are attributed to the interlayer CO_3^{2-} anions, which may result from the reduction of GO and/or the slight dissolution of CO_2 from the air. The peak at 1546 cm^{-1} , corresponding to the skeletal vibration of the carbon ring in the NiCo-LDH-G sample, further confirm the presence of graphene.^[32]

The composition and surface electronic states of ultrathin NiCo-LDH-G nanosheets were further analyzed and examined by X-ray photoelectron spectroscopy (XPS). The results of survey spectra show the ultrathin NiCo-LDH-G nanosheets are composed of Ni, Co, C, O, and Cl elements (Figure S4, Supporting Information), and the metal molar ratio (Ni/Co) of the NiCo-OH and NiCo-LDH-G is calculated to be 1:1 (Table S2, Supporting Information). The high-resolution XPS spectra of Ni 2p are shown in Figure 2c, and the spin-energy separation of the two major peaks that located at 873.5 and 855.9 eV is calculated to be 17.6 eV , indicative of the presence of Ni^{2+} in both NiCo-OH and NiCo-LDH-G samples.^[32,33] However, in the case of the Co 2p high-resolution XPS spectra, the binding energy of the two distinct peaks in the NiCo-LDH-G nanosheets shifts toward lower energy, corresponding to a change in the spin-energy separation from 16.0 eV for the NiCo-OH to 15.4 eV for the NiCo-LDH-G nanosheets (Figure 2d), which is attributed to the presence of Co^{3+} in the NiCo-LDH.^[32,34] These results further confirm that the GO helps to effectively promote the formation of

the NiCo-LDH species via a scheme described below: C/O functional groups on the GO surface contribute to the continuous oxidation from Co^{2+} to Co^{3+} , then the Co^{3+} ions coprecipitate with Ni^{2+} and remaining Co^{2+} ions to form NiCo-LDH instead of β -phase NiCo-OH. The C1s spectrum of the NiCo-LDH-G nanosheets can be fitted into three main peaks, corresponding to the C=C, C–O, and O–C=O, respectively (Figure S5, Supporting Information).^[27,30] This implies that some C/O functional groups still exist on the graphene surface in the NiCo-LDH-G samples, which is beneficial for strong immobilization between the NiCo-LDH nanosheets and the graphene.

To evaluate the valence change of the Ni and Co ions in the two samples, the bulky NiCo-OH plates and the ultrathin NiCo-LDH-G nanosheets were examined by X-ray absorption spectroscopy (XAS). The XAS in total fluorescent yield (TFY) mode can provide valence state information in the bulk (with a probing depth of $\approx 100\text{ nm}$).^[35] We first measured the TFY spectra at the metal Ni and Co L-edges on the as-made NiCo-OH and NiCo-LDH-G samples. Meanwhile, we also acquired the XAS at the Ni and Co L-edges via TEY on the same samples, a measurement that mainly probes changes on the near-surface electronic information (below 10 nm).^[36] The XAS/TFY spectra in Figure 3a reveal that the valence states of bulk Ni ions in both the NiCo-OH and NiCo-LDH-G nanosheets are similar to pure Ni^{2+} , which is consistent with surface data from XAS/TEY results (Figure 3c),^[37,38] implying the uniform distribution of Ni^{2+} in the as-made samples. However, the valence states of Co ions in the NiCo-OH and NiCo-LDH-G nanosheets are appreciably different. In the NiCo-OH samples, the signal from both the bulk and especially from the surface manifests a substantially higher Co^{2+} content (Figure 3b,d, peaks 1, 2, and

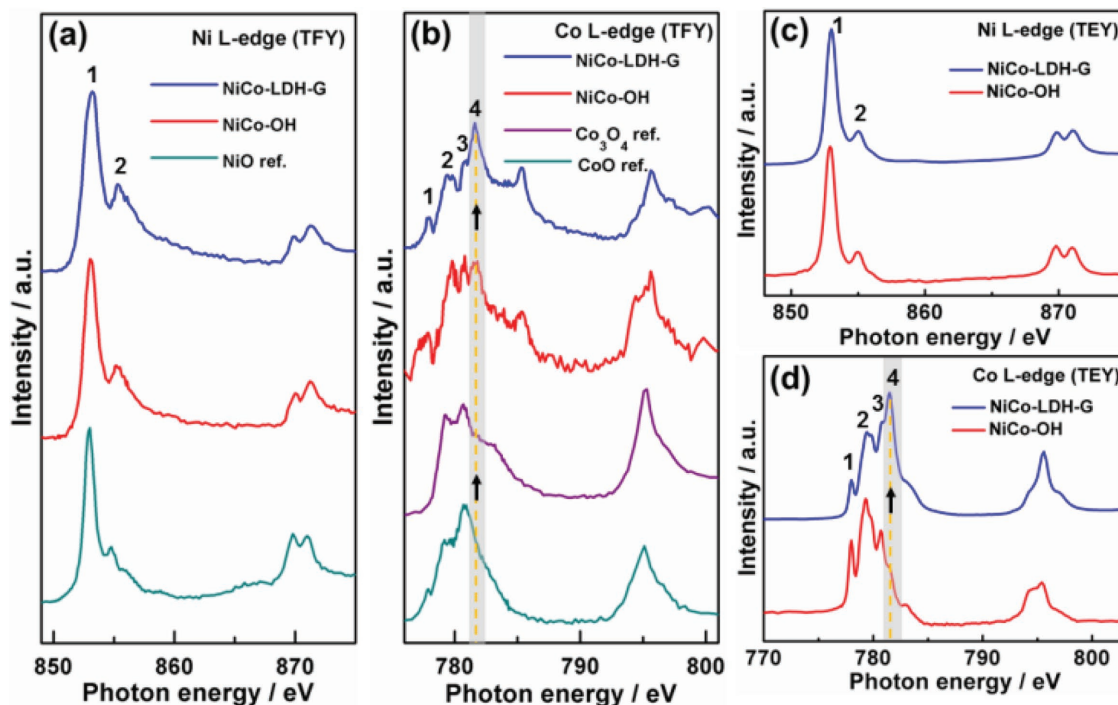


Figure 3. Bulk and surface XAS of bulky NiCo-OH plates and ultrathin NiCo-LDH-G nanosheets: a,b) bulk-sensitive XAS/TFY scans at Ni and Co L-edges; c,d) surface-sensitive XAS/TEY scan at the Ni and Co L-edges.

3). In contrast, in the NiCo-LDH-G nanosheets, both the surface and bulk Co ions are partly oxidized to Co^{3+} , evidenced by an obvious increase of peak 4 intensity. For the O K-edge spectra, two characteristic peaks, prepeak a) and main peak b), assigned to the hybridization of the O 2p with 3d and 4sp orbitals from transition-metal (TM), respectively, are observed (Figure S6, Supporting Information).^[38,39] Compared with the NiCo-OH plates, the spectrum from the NiCo-LDH-G nanosheets shows an obvious drop in the intensity of the prepeak a); such a signature is generally attributed to the in situ formation of abundant oxygen vacancies and the weakening of 3d–2p hybridization.^[39,40] This further suggests that the ultrathin feature of the NiCo-LDH-G nanosheet may result in the rearrangement of the electronic structure of the 3d electron population, thus forms a large number of dangling bonds in the TM surface.^[7] These structural and electronic characteristics provide a positive effect on the OH^- -related electrochemical performance. This kind of structure and electronic nature can effectively facilitate the adsorption of alkaline electrolyte ions, e.g., OH^- on the active sites and directly facilitate electron transfer between surface metal ions and adsorbed intermediates (Figures S7 and S8).^[7,41]

Figure 4 shows the field-emission scanning electron microscopy (FE-SEM) images of the two kinds of structures. As shown in Figure 4a and Figure S9a,b (Supporting Information), the as-obtained NiCo-OH sample in the absence of GO tends to form a re-stacking structure made of the plates with a lateral

size of 3–5 μm . Moreover, these NiCo-OH plates display limited twisting and bending. Interestingly, in sharp contrast with the bulky NiCo-OH plates, a large amount of highly loose and wrinkled nanosheets can be clearly observed in the presence of GO (Figure 4b). The corresponding specific surface area and pore volume of the NiCo-LDH-G nanosheets are as high as 98.3 $\text{m}^2 \text{g}^{-1}$ and 0.47 $\text{cm}^3 \text{g}^{-1}$, respectively (Figure S10 and Table S3, Supporting Information), with an obvious increase in comparison to 29.7 $\text{m}^2 \text{g}^{-1}$ and 0.15 $\text{cm}^3 \text{g}^{-1}$ for NiCo-OH plates. The high-resolution FE-SEM images further reveal the homogenous and full coating of the ultrathin NiCo-LDH nanosheets on the graphene surface (Figure 4c,d), in which the perfect duplication of the GO both in terms of the lateral size and the shape is achieved. It is believed that the GO surface acts as a confined domain and provides a negative electrical field for continued spread growth of the NiCo-LDH seeds. The transmission electron microscopy (TEM) images of the NiCo-LDH-G nanosheets (Figure 4e–g) show a wrinkled and tortuous morphology, indicative of the ultrathin nature of these nanosheets. The TEM images of the NiCo-OH sample are included in Figure S9c,d (Supporting Information), where it is evident that the plates exhibit less tortuosity than the ultrathin nanosheets. These TEM images are consistent with the FE-SEM images of Figure 4a–d. The thickness of the NiCo-LDH-G nanosheets is estimated to be 4.5–4.6 nm based on these folded nanosheet edges, as shown in Figure 4g. The lattice fringes of nanosheet can be observed in a

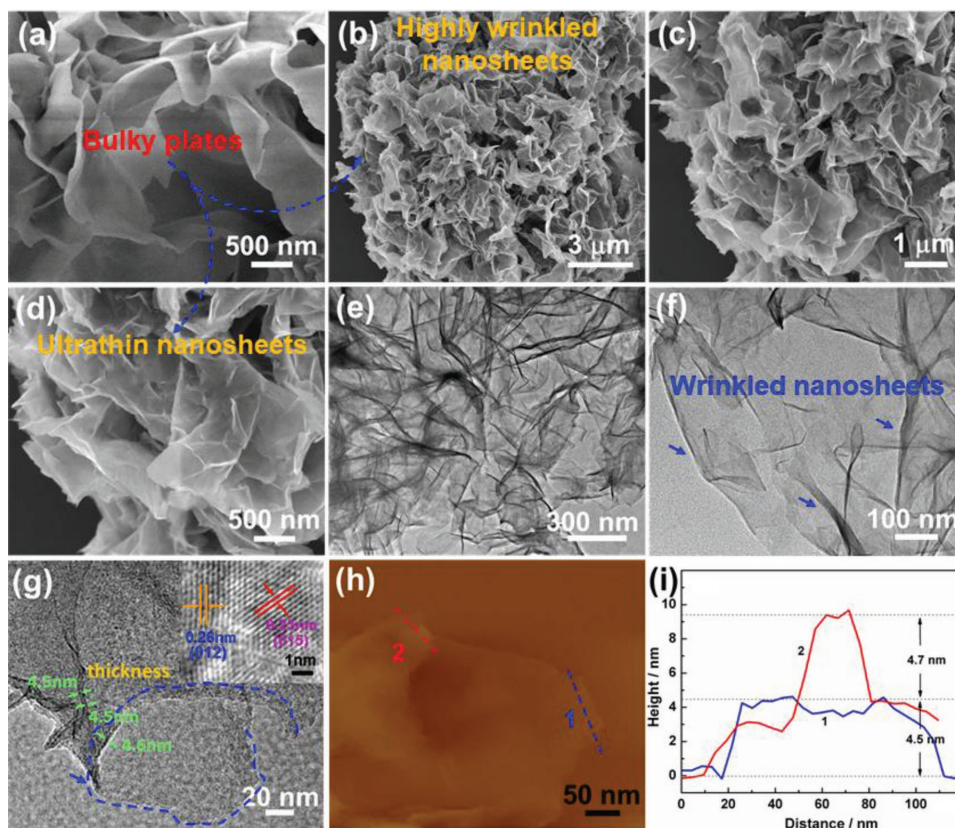


Figure 4. Microstructure characterization of the as-prepared samples: FE-SEM images of a) the bulky NiCo-OH plates and b–d) ultrathin NiCo-LDH-G nanosheets; e–g) TEM and HR-TEM images (inset) of the ultrathin NiCo-LDH-G nanosheets; h) AFM image of the NiCo-LDH-G nanosheets and i) corresponding height profiles.

high-resolution TEM (HR-TEM) image (Figure 4g, inset), with a measured lattice spacing of ≈ 0.23 and 0.26 nm. The two kinds of lattice spacing can be corresponded to the (015) and (012) plane of the LDH phase, respectively. The atomic force microscopy (AFM) measurement results reveal that the thickness of the ultrathin NiCo-LDH-G nanosheets is $4.5\text{--}4.7$ nm (Figure 4h–i), which is consistent with the above TEM results. The corresponding thickness of GO is also measured to be 1.1 nm (Figure S11, Supporting Information), implying that the NiCo-LDH nanosheets with the thickness of $1.7\text{--}1.8$ nm are coated on both sides of the graphene, corresponding to $2\text{--}3$ host layers of the NiCo-LDH with an interplanar spacing of 8.1 Å. This is obviously thinner than the NiCo-OH plates measured with AFM to be 30 nm (Figure S9e,f, Supporting Information). Interestingly, when the concentration of metal salts was increased by a factor of 1.5 , the as-obtained NiCo-LDH-G nanosheets still showed a relatively loose and wrinkled nanosheet structure (Figure S12a–d, Supporting Information), although the corresponding thickness of each nanosheet increased to $7.2\text{--}7.8$ nm (Figure S12e,f, Supporting Information). It is also noted that the crystal structure of these thicker sheets of the NiCo-LDH-G remained unchanged, which is further confirmed by the XRD results (Figure S13, Supporting Information). These findings suggest that the thickness and tortuosity of the NiCo-LDH-G

nanosheets can be well tuned by varying the concentration of metal salt ions.

The scanning transmission electron microscopy with high-angle annular dark-field mode (HAADF-STEM) images further reveal the ultrathin and highly tortuous structure of the NiCo-LDH-G nanosheets (Figure 5a,b and Figure S14, Supporting Information), which is consistent with the FE-SEM and bright-field TEM results. Furthermore, electron energy-loss spectroscopy (EELS) line profiles on the samples were also analyzed for composition homogeneity. For the Co and Ni L-edge spectra (Figure 5c), there are no noticeable changes in the integrated intensity ratio of the L3 to L2 peaks, suggesting the homogeneous distribution of Co and Ni ions on the NiCo-LDH-G nanosheets. Meanwhile, the O K-edge spectra as shown in Figure 5d, the characteristic prepeak near the edge onset shows a similar trend with the XAS results; there is a reduction in the pre-peak intensity in comparison to that of the NiCo-OH (Figure S15, Supporting Information), which further confirms the electronic structural change of the TM surroundings in the ultrathin nanosheet structures. The corresponding energy dispersive spectroscopy (EDS) elemental maps of the NiCo-LDH nanosheets (Figure 5e–j) show the distribution of C, Co, Ni, O, and Cl elements, indicative of the homogeneous composition in the NiCo-LDH nanosheets on the graphene. It is noted that the Cl is mainly attributed to

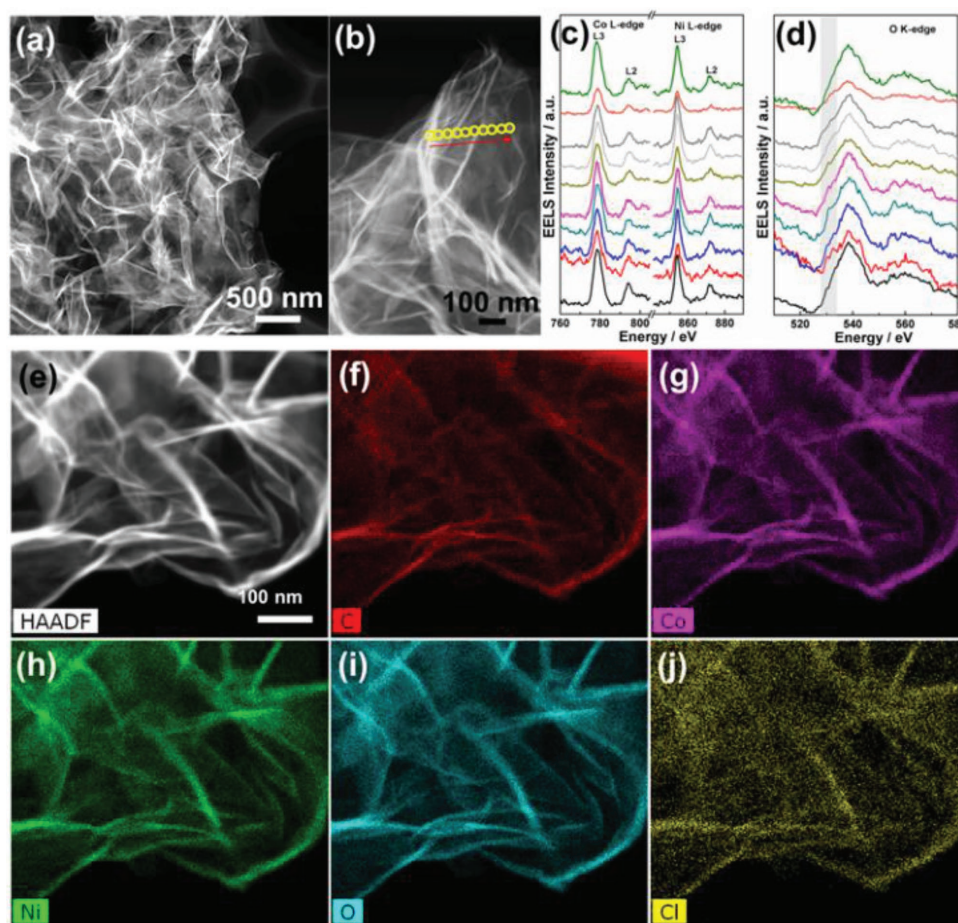


Figure 5. Microstructure characterization of the ultrathin and highly tortuous NiCo-LDH-G nanosheets: a,b) HAADF-STEM images; c) L-edge (Co and Ni) and d) K-edge (O) EELS spectra; f–j) EDS elemental maps (K-edge) of C, Co, Ni, O, and Cl from the image (e).

the intercalated anions (Cl^-) of the NiCo-LDH phase, this is also confirmed by the lower content of Cl in the NiCo-OH plates (Figure S16, Supporting Information). The mixed EDS elemental mapping further shows that the Ni and Co distribute throughout the entire nanosheet, which further indicates the formation of the homogeneous nanostructure in the NiCo-LDH nanosheets (Figure S17, Supporting Information).

To gain further insight into the formation and growth mechanism of ultrathin NiCo-LDH nanosheets, monometallic compound-G hybrids were fabricated in the presence of GO, but with a single metal salt, $\text{NiCl}_2 \cdot 6\text{H}_2\text{O}$ or $\text{CoCl}_2 \cdot 6\text{H}_2\text{O}$. These two samples are named as $\text{Ni}(\text{OH})_2\text{-G}$ and $\text{Co}_i\text{Co}_{ii}\text{-LDH}/\text{Co}_3\text{O}_4\text{-G}$, respectively, and the characterization results are shown in Figure S18 (Supporting Information). The XRD patterns reveal that the diffraction peaks of the as-obtained $\text{Ni}(\text{OH})_2\text{-G}$ sample can be assigned to (001), (100), and (102) plane reflections of typical $\beta\text{-Ni}(\text{OH})_2$ (Figure S18a, Supporting Information). In comparison to that of the $\text{Ni}(\text{OH})_2\text{-G}$ hybrids, the diffraction peaks of the Co-based compound-G hybrids ($\text{Co}_i\text{Co}_{ii}\text{-LDH}/\text{Co}_3\text{O}_4\text{-G}$) are composed of LDH and metal oxide phases, specifically $\text{Co}_i\text{Co}_{ii}\text{-LDH}$ (Co_i and Co_{ii} represent Co^{2+} and Co^{3+} , respectively) and Co_3O_4 . To further understand the unique role of GO, the monometallic Co-based compound in the absence of the GO was also synthesized, which mainly reveals the presence of the $\beta\text{-Co}(\text{OH})_2$ phase (Figure S19, Supporting Information). These results show that the GO has played a critical role in the continuous oxidation of Co^{2+} to Co^{3+} , which is also consistent with the aforementioned XAS and high-resolution XPS results. This means that the GO is only sensitive to Co^{2+} ions in the present work. Furthermore, the FE-SEM images show the $\text{Ni}(\text{OH})_2\text{-G}$ hybrids tend to be bulky and aggregated structures, however, it is difficult to define the ultrathin nanosheets due to a great deal of $\text{Ni}(\text{OH})_2$ species accumulated on the graphene surface (Figure S18b,c, Supporting Information). For the $\text{Co}_i\text{Co}_{ii}\text{-LDH}/\text{Co}_3\text{O}_4\text{-G}$ hybrids, heterogeneous and disordered nanostructures made of some nanosheets and bulky cubes are clearly observed (Figure S18d, Supporting Information). The high-magnification FE-SEM image further reveals the formation of relatively thick graphene-based hybrid nanosheets, which is due to the overcoating of $\text{Co}_i\text{Co}_{ii}\text{-LDH}$ on the graphene surface (Figure S18e, Supporting Information). The bulky species with the cubic shape can be assigned to Co_3O_4 phase that is formed by deep oxidation of C/O functional groups on GO surface (Figure S18f, Supporting Information); the cubic shape is a stable structure of this kind of metal oxide.^[42] Based on the above results, it is not difficult for one to conclude that the continuous oxidation of the Co^{2+} ions on the surface of the GO leads to the in situ formation of the LDH seeds. Subsequently, the electrostatic interaction plays a pivotal role in confining the nanoscale growth of homogenous ultrathin LDH nanosheets on the graphene surface. Additionally, the synergistic effects of binary metal ions, i.e., Ni^{2+} and Co^{2+} , also ensure the formation of LDH nanosheets with ultrathin features.

2.2. Electrochemical Performance of Ultrathin NiCo-LDH-G Nanosheets

The ultrathin and highly tortuous NiCo-LDH-G nanosheets were evaluated for their potential as electrocatalyst or supercapacitor

electrodes. It has been found that the as-obtained materials exhibit fast reaction kinetics, high electrocatalytic activity and excellent charge storage capability. These desirable properties arise in part from the large electrochemically active surface and the short path lengths for fast ion and electron transport.

The electrochemical activity of the ultrathin NiCo-LDH-G nanosheets for catalytic OER was evaluated in alkaline solution (0.1 M KOH). The linear sweep voltammetry (LSV) curves of as-made samples were shown in Figure 6a (ohmic potential drop was corrected, Figure S20, Supporting Information), from which one can see that the ultrathin NiCo-LDH-G nanosheet catalysts have the lowest onset potential of 1.495 V versus RHE and the highest current density as the potential increases. It is noted that the peaks near 1.35–1.40 V are related to the following two reactions: $\text{M}^{2+}(\text{OH})_2 \rightarrow \text{M}^{3+}\text{OOH}$ and $\text{M}^{3+}\text{OOH} \rightarrow \text{M}^{4+}\text{O}_2$ (M represents Ni and Co).^[43] It is believed that the $\text{M}^{3+/4+}$ species, which are formed in situ, can promote the formation and de-protonation of the intermediate species (OOH), and finally give rise to O_2 evolution; this step is particularly critical to enhance the OER performance. As seen from Figure S20 (Supporting Information), the peak intensity of the NiCo-LDH-G nanosheet electrodes is higher than that of the bulky NiCo-OH plate electrodes, indicating that the wider interlayer spacing of the NiCo-LDH-G creates abundant active sites for the electrochemical reaction. Remarkably, the ultrathin NiCo-LDH-G nanosheets show a lower overpotential (η) of 0.337 V at the current density of 10 mA cm^{-2} , in comparison to that of some other common catalysts (Figure 6b). These electrochemical performances are comparable, and even superior to those of the Co/Ni-based hydroxide catalysts reported recently in literature under the same electrolyte solution (0.1 M KOH or NaOH) and even 1 M KOH solution (Table S4, Supporting Information).^[16,28,44–50]

Figure 6c shows the Tafel plots of the as-prepared samples, in which the ultrathin NiCo-LDH-G nanosheet electrode exhibits a Tafel slope of 52 mV dec^{-1} . This value is smaller than those of NiCo-OH (78 mV dec^{-1}), Pt/C (101 mV dec^{-1}), and RuO_2 (68 mV dec^{-1}), suggesting the excellent intrinsic reaction kinetics of the NiCo-LDH nanosheets. In addition, the mass activity of the NiCo-LDH-G nanosheets is also obviously higher than the pristine NiCo-OH plates at various overpotentials (Figure 6d), implying a highly effective exploitation of active species. The catalytic stability of the NiCo-LDH-G was also evaluated at the overpotential of 0.337 V for 4 h (Figure 6e). It was found that the ultrathin NiCo-LDH-G nanosheets can retain a high catalytic activity for long-time testing. It is noted that the slight current increase during the first 30 min may be due to the wettability effects of electrode materials. The high stability is also confirmed by chronopotentiometric tests for 12 h (Figure S21, Supporting Information). The electrochemical impedance spectra (EIS) results further reveal a decreased intrinsic resistance and ion transport resistance in the ultrathin NiCo-LDH-G nanosheets (Figure 6f). These results have clearly demonstrated that the ultrathin and highly tortuous structures of NiCo-LDH-G nanosheets can strongly improve the catalytic OER performance.

As a proof-of-concept application, the electrochemical performance of the ultrathin NiCo-LDH-G nanosheets for supercapacitors was also evaluated. Figure 7a shows the cyclic voltammetry (CV) curves for the bulky NiCo-OH plates and ultrathin NiCo-LDH-G nanosheet electrodes at a scan rate (v)

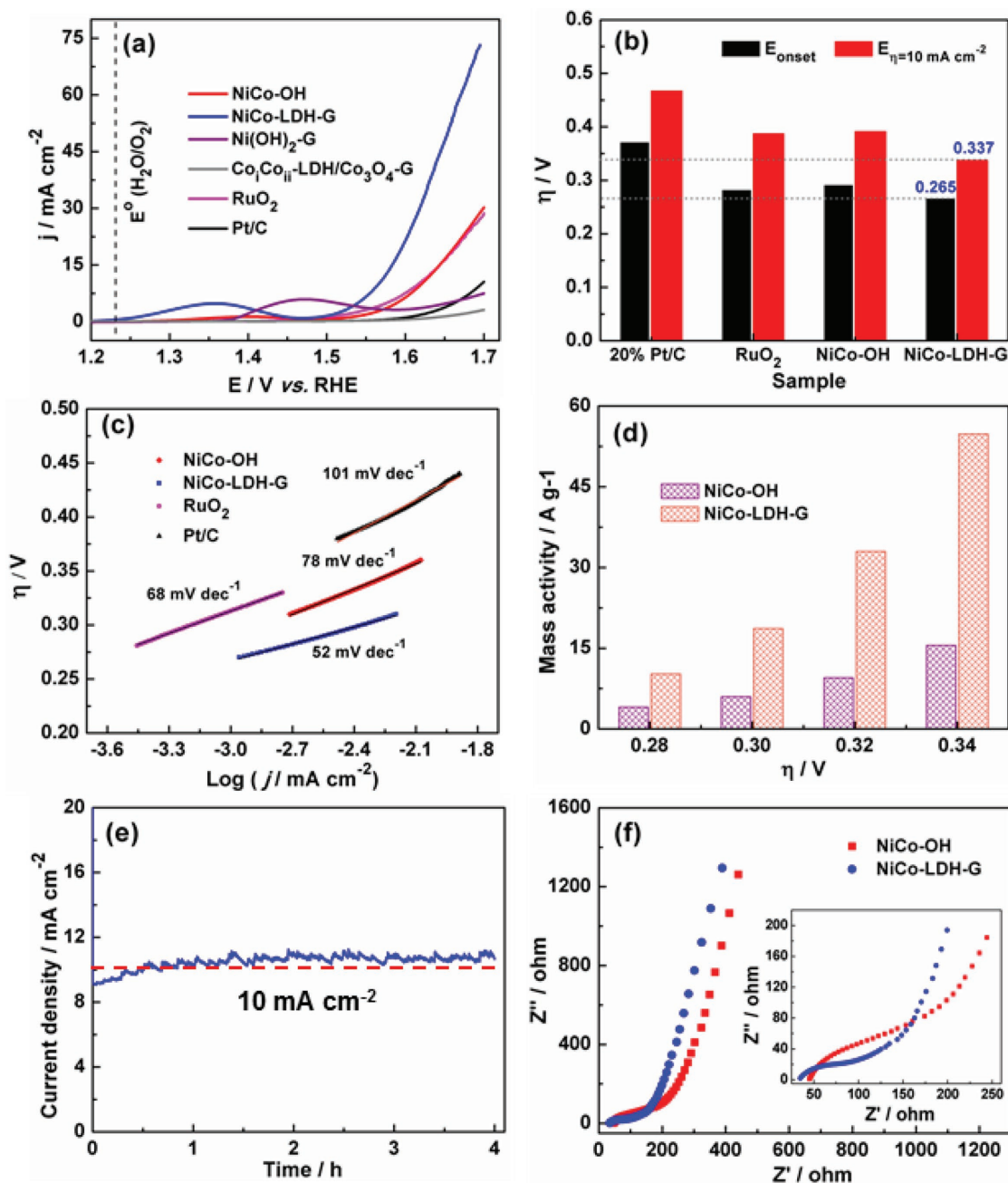


Figure 6. Electrochemical activity of the as-prepared samples for catalytic OER: a) the LSV curves of the bulky NiCo-OH plates, ultrathin NiCo-LDH-G nanosheets, Ni(OH)₂-G, Co₂Co₃-LDH/Co₃O₄-G, Pt/C catalyst and the RuO₂ catalyst at a scan rate of 10 mV s⁻¹ with iR compensation; b) onset potentials and overpotentials at a current density of 10 mA cm⁻²; c) Tafel plots of the various samples at the scan rate of 0.1 mV s⁻¹; d) mass activity of the pristine NiCo-OH and NiCo-LDH-G nanosheets; e) the catalytic stability of the ultrathin NiCo-LDH-G nanosheets at the overpotential of 0.337 V; f) EIS of the bulky NiCo-OH plates and ultrathin NiCo-LDH-G nanosheets.

of 10 mV s⁻¹, in which a pair of redox peaks related to M(OH)₂/MOOH/MO₂ are presented. Moreover, the peak current densities (*I*_p) of the ultrathin NiCo-LDH-G nanosheet electrodes are larger than that of the bulk NiCo-OH plate electrodes (Figure 7b and Figure S22, Supporting Information), indicating that the ultrathin NiCo-LDH-G nanosheets have a fast kinetics process; this was further confirmed by EIS spectroscopy (Figure S23, Supporting Information). The kinetic processes of the bulky

NiCo-OH and ultrathin NiCo-LDH-G samples were further evaluated at different scan rates ranging from 0.5 to 50 mV s⁻¹ (Figure S24, Supporting Information). It can be clearly seen that the slope of the linear plot from log *I*_p versus log *v* for both the NiCo-LDH-G and the NiCo-OH electrodes are nearly the same. The slope is ≈1 at low scan rates ranging from 0.5 to 2 mV s⁻¹, indicating that the kinetics are dominated by the surface electrochemical reactions.^[51,52] Nevertheless, the

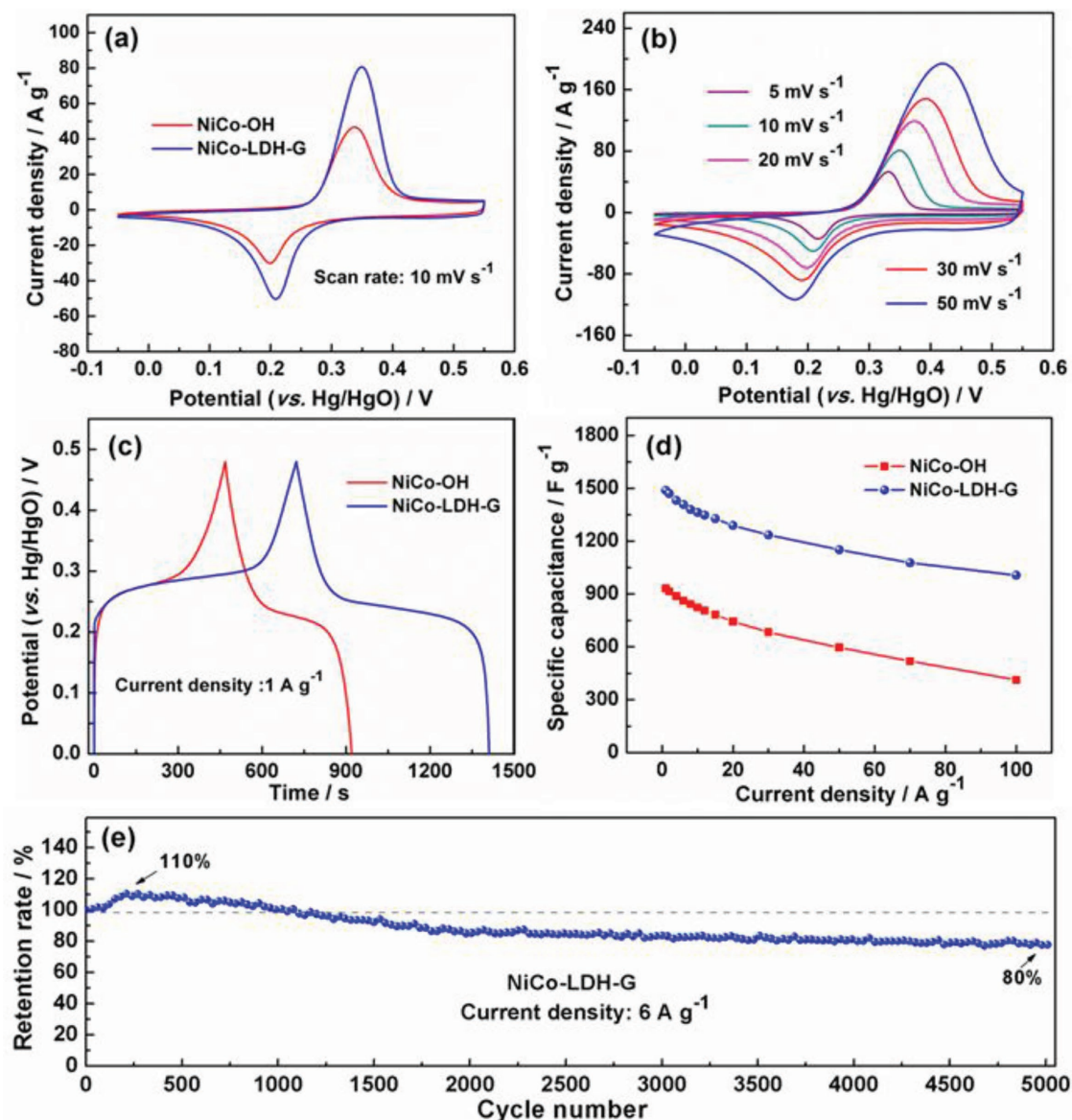


Figure 7. Electrochemical performance of the bulky NiCo-OH plates and ultrathin NiCo-LDH-G nanosheets for supercapacitors: a) CV curves of the bulky NiCo-OH plates and ultrathin NiCo-LDH-G nanosheets at 10 mV s^{-1} ; b) CV curves of the ultrathin NiCo-LDH-G nanosheets at different scan rates ranging from 5 to 50 mV s^{-1} ; c) charge/discharge curves of the bulky NiCo-OH plates and ultrathin NiCo-LDH-G nanosheets at 1 A g^{-1} ; d) the specific capacitance of the bulky NiCo-OH plates and ultrathin NiCo-LDH-G nanosheets at different current densities ranging from 1 to 100 A g^{-1} ; and e) the cycling performance of the ultrathin NiCo-LDH-G nanosheets at 6 A g^{-1} .

slope of the NiCo-OH and NiCo-LDH-G nanosheet electrode is reduced to 0.6–0.7 at high scan rates ($2\text{--}50 \text{ mV s}^{-1}$), implying that the electron and electrolyte ion transfer/diffusion gradually become the rate-limiting step of the charge storage. It should be noted that the surface capacitive and diffusion contribution to the total charge storage can be further quantified (Figure S25, Supporting Information). The ratio of the capacitive contribution of the NiCo-LDH-G nanosheet electrode is calculated to be 62.1% at a scan rate of 0.5 mV s^{-1} , and even as high as 89.4% at a scan rate of 10 mV s^{-1} , indicating a fast electron and ion transport in the ultrathin and highly tortuous hybrid structures. The specific capacitance based on the charge-discharge curves (Figure 7c and Figure S26, Supporting Information), is shown

in Figure 7d. The NiCo-LDH-G electrodes can deliver a high specific capacitance of 1489 F g^{-1} , higher than 932 F g^{-1} of the NiCo-OH at a current density of 1 A g^{-1} , and a capacitance retention rate of 68% (1007 F g^{-1} at 100 A g^{-1}) can be achieved, this is obvious superior to those of the other NiCo-hydroxide materials as reported previously.^[53–56] Such a remarkable high-rate performance can be ascribed to the relatively wide inter-layer distance and the ultrathin and highly tortuous structures of NiCo-LDH-G nanosheets with the large specific surface area and multilevel pore structure, which provides numerous channels for the access of electrolyte ions, thus leading to the fast reaction kinetics. In addition, the high electrical conductivity of the NiCo-LDH-G nanosheet electrodes due to the incorporation

of graphene also delivers a fast electron transport. Benefiting from these advantages, the ultrathin NiCo-LDH-G nanosheet electrodes also keep an excellent electrochemical stability of $\approx 80\%$ at 6 A g^{-1} for 5000 cycles (Figure 6e). It is found that the specific capacitance is increased by 10% of its initial capacitance during the first 200 cycles, which may be related to the electrochemical activation of electrode materials.

3. Conclusion

In summary, we have developed a GO surface-confined strategy for fabrication of ultrathin and highly tortuous NiCo-LDH-G nanosheets, where the C/O functional groups on the GO surface promote the oxidation of Co^{2+} to Co^{3+} , and induce transformation of the NiCo-OH from the β -phase to the LDH-phase, resulting in the homogenous and guided-growth of the ultrathin NiCo-LDH nanosheets on the graphene surface. By duplicating the large surface of the graphene substrate, the as-obtained NiCo-LDH-G nanosheets feature ultrathin and highly wrinkled structures. It has demonstrated that the NiCo-LDH-G nanosheets show a high electrochemical activity for catalytic OER and an excellent charge storage capability for supercapacitors. This work may open a new way for the controlled fabrication of ultrathin 2D materials with tuned structure for energy-storage and energy-conversion.

4. Experimental Section

Surface-Confined Fabrication of Ultrathin NiCo-LDH Nanosheets: All of the chemical reagents with analytical purity were directly used as received. In a typical run, the as-exfoliated GO (30 mg) was dispersed into the water of 250 mL to form a dispersion solution under continuous ultrasonication. Subsequently, 1 mmol nickel chloride hexahydrate ($\text{NiCl}_2 \cdot 6\text{H}_2\text{O}$), 1 mmol cobalt chloride hexahydrate ($\text{CoCl}_2 \cdot 6\text{H}_2\text{O}$), and 8.75 mmol hexamethylenetetramine (HMT) were added into the above solution under vigorous stirring. The solution was refluxed at 95°C for 5 h in an oil bath, and then the precipitates were collected by centrifugation for several times with water and alcohol. The samples were dried at 80°C overnight to obtain NiCo-LDH-G nanosheets. For comparison, the bulky NiCo-OH samples without GO were also obtained under the same conditions. Other metal compound-G hybrids, namely, $\text{Ni}(\text{OH})_2\text{-G}$ and $\text{Co}_x\text{Co}_y\text{-LDH}/\text{Co}_3\text{O}_4\text{-G}$, were also prepared in the presence of single metal salt $\text{NiCl}_2 \cdot 6\text{H}_2\text{O}$ or $\text{CoCl}_2 \cdot 6\text{H}_2\text{O}$, respectively.

Materials Characterization: The structures and morphologies of as-obtained samples were examined by XRD (Cu $K\alpha$, $\lambda = 1.5406 \text{ \AA}$), FE-SEM (FEI NOVA NanoSEM 450), and TEM (FEI Tecnai G2 F30 and T20). The FEI Titan instrument with EDS was used for elemental analysis. The XPS, XAS, and EELS were performed to analyze the chemical bonding states. The thickness of the samples was determined by AFM. The surface structural information was detected by FT-IR and Raman spectroscopy.

Electrochemical Characterization: The electrochemical measurements were carried out on CHI 760D electrochemical workstation in a standard three-electrode system. For the OER, the working electrode was prepared according to our previous work.^[57] 4 mg catalyst was added to 1 mL mixture solution of ethanol and Nafion (5 wt%) to form a homogeneous ink. Then, the catalyst ink was coated onto a glassy carbon electrode with a loading of 0.20 mg cm^{-2} . The Pt wire and Ag/AgCl were applied as the counter and reference electrodes, respectively. All potentials measured were calibrated versus RHE by $E_{(\text{RHE})} = E_{(\text{Ag}/\text{AgCl})} + 0.059 \times \text{pH} + 0.197$, in 0.1 M KOH electrolyte. The LSV curves were measured at a scan rate of 0.1 and 10 mV s^{-1} , respectively. All LSV curves were corrected with

iR-compensation. The mass activity (A g^{-1}) of the sample was calculated from the loading m (mg cm^{-2}) and the current density j (mA cm^{-2}) at the overpotential η (for example, $\eta = 300 \text{ mV}$)

$$\text{Mass activity} = j/m \quad (1)$$

The electrochemical stability of the sample was recorded at the overpotential $\eta = 0.337 \text{ V}$ and the current density of 2 mA cm^{-2} , respectively.

For supercapacitors, the working electrode was fabricated as following: the mixture slurry of active materials (80%), carbon black (10%), and polyvinylidene fluoride (10%) was coated on the current collectors, and then the electrode was vacuum dried at 120°C for 12 h. The mass loading of samples on the current collector was calculated to be 2.0 mg cm^{-2} . The counter and reference electrodes were Pt foil and Hg/HgO electrodes, respectively, with 6 M KOH aqueous solution as the electrolyte. The CV curves were measured by sweeping from the potential of 0–0.55 V at various scan rates. The specific capacitance (C_s , F g^{-1}) of the sample was evaluated by the following equation^[58]

$$C_s = I/m(dV/dt) \quad (2)$$

Here, I is the current density (A g^{-1}), dV/dt is the gradient of the discharge curve (V s^{-1}), and m is the loading mass of the electrodes (g).

Supporting Information

Supporting Information is available from the Wiley Online Library or from the author.

Acknowledgements

This work was partly supported by the National Natural Science Foundation of China (Nos. 21336001, 51802251), the China Postdoctoral Science Foundation (No. 2018M631168), and the Fundamental Research Funds for the Central Universities (No. xjj2018036). H.Z. thanks the funding support from U.S. Department of Energy, Office of Science, Office of Basic Energy Sciences, Materials Sciences and Engineering Division under Contract No. DE-AC02-05-CH11231 within the KC22ZH program. J.Y. acknowledges the support from the Chinese Scholarship Council (No. 201506060073). Work at the Molecular Foundry was supported by the Office of Science, Office of Basic Energy Sciences, the U.S. Department of Energy under Contract No. DE-AC02-05CH11231.

Conflict of Interest

The authors declare no conflict of interest.

Keywords

graphene-guided growth, NiCo-layered double hydroxides, oxygen evolution reaction, supercapacitors, ultrathin nanosheets

Received: May 11, 2018

Revised: August 11, 2018

Published online: September 14, 2018

[1] Y. Sun, S. Gao, F. Lei, Y. Xie, *Chem. Soc. Rev.* **2015**, *44*, 623.

[2] C. L. Tan, X. H. Cao, X. J. Wu, Q. Y. He, J. Yang, X. Zhang, J. Z. Chen, W. Zhao, S. K. Han, G. H. Nam, M. Sindoro, H. Zhang, *Chem. Rev.* **2017**, *117*, 6225.

- [3] K. Rui, G. Zhao, Y. Chen, Y. Lin, Q. Zhou, J. Chen, J. Zhu, W. Sun, W. Huang, S. X. Dou, *Adv. Funct. Mater.* **2018**, *28*, 1801554.
- [4] S. Gao, Y. Lin, X. Jiao, Y. Sun, Q. Luo, W. Zhang, D. Li, J. Yang, Y. Xie, *Nature* **2016**, *529*, 68.
- [5] G. Zhang, H. Liu, J. Qu, J. Li, *Energy Environ. Sci.* **2016**, *9*, 1190.
- [6] Y. Zhao, G. Chen, T. Bian, C. Zhou, G. I. Waterhouse, L. Z. Wu, C. H. Tung, L. J. Smith, D. O'Hare, T. Zhang, *Adv. Mater.* **2015**, *27*, 7824.
- [7] J. Huang, J. Chen, T. Yao, J. He, S. Jiang, Z. Sun, Q. Liu, W. Cheng, F. Hu, Y. Jiang, Z. Pan, S. Wei, *Angew. Chem., Int. Ed.* **2015**, *54*, 8722.
- [8] S. Gao, Y. Sun, F. Lei, L. Liang, J. Liu, W. Bi, B. Pan, Y. Xie, *Angew. Chem., Int. Ed.* **2014**, *53*, 12789.
- [9] J. Chen, B. Liu, Y. Liu, W. Tang, C. T. Nai, L. Li, J. Zheng, L. Gao, Y. Zheng, H. S. Shin, H. Y. Jeong, K. P. Loh, *Adv. Mater.* **2015**, *27*, 6722.
- [10] X. Duan, C. Wang, J. C. Shaw, R. Cheng, Y. Chen, H. Li, X. Wu, Y. Tang, Q. Zhang, A. Pan, J. Jiang, R. Yu, Y. Huang, X. Duan, *Nat. Nanotechnol.* **2014**, *9*, 1024.
- [11] C. Tan, H. Zhang, *J. Am. Chem. Soc.* **2015**, *137*, 12162.
- [12] M. R. Lukatskaya, O. Mashtalir, C. E. Ren, Y. Dall'Agnese, P. Rozier, P. L. Taberna, M. Naguib, P. Simon, M. W. Barsoum, Y. Gogotsi, *Science* **2013**, *341*, 1502.
- [13] S. Gao, X. Jiao, Z. Sun, W. Zhang, Y. Sun, C. Wang, Q. Hu, X. Zu, F. Yang, S. Yang, L. Liang, J. Wu, Y. Xie, *Angew. Chem., Int. Ed.* **2016**, *55*, 698.
- [14] L. Wang, C. Lin, F. Zhang, J. Jin, *ACS Nano* **2014**, *8*, 3724.
- [15] B. Zhao, L. Zhang, Q. Zhang, D. Chen, Y. Cheng, X. Deng, Y. Chen, R. Murphy, X. Xiong, B. Song, C. P. Wong, M. S. Wang, M. Liu, *Adv. Energy Mater.* **2018**, *8*, 1702247.
- [16] Y. Dou, L. Zhang, J. Xu, C. T. He, X. Xu, Z. Sun, T. Liao, B. Nagy, P. Liu, S. X. Dou, *ACS Nano* **2018**, *12*, 1878.
- [17] F. Song, X. Hu, *J. Am. Chem. Soc.* **2014**, *136*, 16481.
- [18] S. Yang, Y. Liu, Y. Hao, X. Yang, W. A. Goddard, X. L. Zhang, B. Cao, *Adv. Sci.* **2018**, *5*, 1700659.
- [19] L. Wei, H. E. Karahan, S. Zhai, H. Liu, X. Chen, Z. Zhou, Y. Lei, Z. Liu, Y. Chen, *Adv. Mater.* **2017**, *29*, 1701410.
- [20] J. Yang, C. Yu, X. Fan, S. Liang, S. Li, H. Huang, Z. Ling, C. Hao, J. Qiu, *Energy Environ. Sci.* **2016**, *9*, 1299.
- [21] S. Li, D. Wu, C. Cheng, J. Wang, F. Zhang, Y. Su, X. Feng, *Angew. Chem., Int. Ed.* **2013**, *52*, 12105.
- [22] Y. Liang, H. Wang, J. Zhou, Y. Li, J. Wang, T. Regier, H. Dai, *J. Am. Chem. Soc.* **2012**, *134*, 3517.
- [23] P. Xiong, B. Liu, V. Teran, Y. Zhao, L. Peng, X. Wang, G. Yu, *ACS Nano* **2014**, *8*, 8610.
- [24] R. Ma, J. Liang, X. Liu, T. Sasaki, *J. Am. Chem. Soc.* **2012**, *134*, 19915.
- [25] L. Wang, Z. H. Dong, Z. G. Wang, F. X. Zhang, J. Jin, *Adv. Funct. Mater.* **2013**, *23*, 2758.
- [26] G. Zhou, D. W. Wang, L. C. Yin, N. Li, F. Li, H. M. Cheng, *ACS Nano* **2012**, *6*, 3214.
- [27] C. Yu, J. Yang, C. Zhao, X. Fan, G. Wang, J. Qiu, *Nanoscale* **2014**, *6*, 3097.
- [28] C. Tang, H. S. Wang, H. F. Wang, Q. Zhang, G. L. Tian, J. Q. Nie, F. Wei, *Adv. Mater.* **2015**, *27*, 4516.
- [29] Z. Liu, R. Ma, M. Osada, K. Takada, T. Sasaki, *J. Am. Chem. Soc.* **2005**, *127*, 13869.
- [30] J. Yang, C. Yu, X. Fan, C. Zhao, J. Qiu, *Adv. Funct. Mater.* **2015**, *25*, 2109.
- [31] Z. P. Xu, H. C. Zeng, *Chem. Mater.* **1999**, *11*, 67.
- [32] J. Yang, C. Yu, X. Fan, Z. Ling, J. Qiu, Y. Gogotsi, *J. Mater. Chem. A* **2013**, *1*, 1963.
- [33] J. Yang, C. Yu, X. Fan, J. Qiu, *Adv. Energy Mater.* **2014**, *4*, 1400761.
- [34] X. Wang, C. Yan, A. Sumboja, J. Yan, P. S. Lee, *Adv. Energy Mater.* **2014**, *4*, 1301240.
- [35] H. Wadati, A. J. Achkar, D. G. Hawthorn, T. Z. Regier, M. P. Singh, K. D. Truong, P. Fournier, G. Chen, T. Mizokawa, G. A. Sawatzky, *Appl. Phys. Lett.* **2012**, *100*, 193906.
- [36] B. Zhang, X. Zheng, O. Voznyy, R. Comin, M. Bajdich, M. García-Melchor, L. Han, J. Xu, M. Liu, L. Zheng, F. P. García de Arquer, C. T. Dinh, F. Fan, M. Yuan, E. Yassitepe, N. Chen, T. Regier, P. Liu, Y. Li, P. De Luna, A. Janmohamed, H. L. Xin, H. Yang, A. Vojvodic, E. H. Sargent, *Science* **2016**, *352*, 333.
- [37] L. Soriano, A. Gutiérrez, I. Preda, S. Palacín, J. M. Sanz, M. Abbate, J. F. Trigo, A. Vollmer, P. R. Bressler, *Phys. Rev. B* **2006**, *74*, 193402.
- [38] F. Lin, D. Nordlund, T. C. Weng, Y. Zhu, C. Ban, R. M. Richards, H. L. Xin, *Nat. Commun.* **2014**, *5*, 3358.
- [39] J. Wang, J. Zhou, Y. Hu, T. Regier, *Energy Environ. Sci.* **2013**, *6*, 926.
- [40] J. H. Kwon, W. S. Choi, Y. K. Kwon, R. Jung, J. M. Zuo, H. N. Lee, M. Kim, *Chem. Mater.* **2014**, *26*, 2496.
- [41] J. Suntivich, K. J. May, H. A. Gasteiger, J. B. Goodenough, S. Yang Horn, *Science* **2011**, *334*, 1383.
- [42] X. Xiao, X. Liu, H. Zhao, D. Chen, F. Liu, J. Xiang, Z. Hu, Y. Li, *Adv. Mater.* **2012**, *24*, 5762.
- [43] G. Liu, P. Li, G. Zhao, X. Wang, J. Kong, H. Liu, H. Zhang, K. Chang, X. Meng, T. Kako, J. Ye, *J. Am. Chem. Soc.* **2016**, *138*, 9128.
- [44] K. Fan, H. Chen, Y. Ji, H. Huang, P. M. Claesson, Q. Daniel, B. Philippe, H. Rensmo, F. Li, Y. Luo, L. Sun, *Nat. Commun.* **2016**, *7*, 11981.
- [45] M. Gao, W. Sheng, Z. Zhuang, Q. Fang, S. Gu, J. Jiang, Y. Yan, *J. Am. Chem. Soc.* **2014**, *136*, 7077.
- [46] H. Liang, F. Meng, M. Cabán Acevedo, L. Li, A. Forticaux, L. Xiu, Z. Wang, S. Jin, *Nano Lett.* **2015**, *15*, 1421.
- [47] J. Nai, H. Yin, T. You, L. Zheng, J. Zhang, P. Wang, Z. Jin, Y. Tian, J. Liu, Z. Tang, L. Guo, *Adv. Energy Mater.* **2015**, *5*, 1401880.
- [48] Z. Li, F. Han, C. Li, X. Jiao, D. Chen, *Chem. Asian J.* **2018**, *13*, 1129.
- [49] T. Tang, W.-J. Jiang, S. Niu, N. Liu, H. Luo, Q. Zhang, W. Wen, Y.-Y. Chen, L.-B. Huang, F. Gao, J.-S. Hu, *Adv. Funct. Mater.* **2018**, *28*, 1704594.
- [50] J. Liu, Y. Ji, J. Nai, X. Niu, Y. Luo, L. Guo, S. Yang, *Energy Environ. Sci.* **2018**, *11*, 1736.
- [51] V. Augustyn, J. Come, M. A. Lowe, J. W. Kim, P.-L. Taberna, S. H. Tolbert, H. D. Abruña, P. Simon, B. Dunn, *Nat. Mater.* **2013**, *12*, 518.
- [52] M. Sathiy, A. S. Prakash, K. Ramesha, J. M. Tarascon, A. K. Shukla, *J. Am. Chem. Soc.* **2011**, *133*, 16291.
- [53] X. Li, H. Wu, A. M. Elshahawy, L. Wang, S. J. Pennycook, C. Guan, J. Wang, *Adv. Funct. Mater.* **2018**, *28*, 1800036.
- [54] G. Yilmaz, K. M. Yam, C. Zhang, H. J. Fan, G. W. Ho, *Adv. Mater.* **2017**, *29*, 1606814.
- [55] Z. Lv, Q. Zhong, Y. Bu, *Adv. Mater. Interfaces* **2018**, *5*, 1800438.
- [56] H. N. Ma, J. He, D. B. Xiong, J. S. Wu, Q. Q. Li, V. Dravid, Y. F. Zhao, *ACS Appl. Mater. Interfaces* **2016**, *8*, 1992.
- [57] J. Yang, C. Yu, S. Liang, S. Li, H. Huang, X. Han, C. Zhao, X. Song, C. Hao, P. M. Ajayan, J. Qiu, *Chem. Mater.* **2016**, *28*, 5855.
- [58] L. Q. Mai, A. M. Khan, X. Tian, K. M. Hercule, Y. L. Zhao, X. Lin, X. Xu, *Nat. Commun.* **2013**, *4*, 2923.